terrestrial atmosphere (Fig. 1), suggesting that opaque grains and matrix portions are poor in subsolar gas. On the other hand, one matrix portion (4Mx in Table 1) shows a high ^{132}Xe concentration along with elemental ratios essentially identical to those of 'Q-gas'—this indicates that residual 'phase-Q' is located in the matrix portion, as in other chondrite classes[2].

How were large amounts of noble gases trapped in chondrules and retained within the chondrule-forming minerals? Implantation of high-energy particles from the young Sun would explain the high ^{36}Ar concentration in silicate materials, as in the case of lunar soils abundant in solar gases[7]. For example, the 'X-wind' model[15] proposed particle irradiation in the early Solar System. Our estimate predicts that diffusive loss[16] of solar-type noble gases from silicate melt can explain ^{20}Ne/^{36}Ar/^{132}Xe ratios and abundances of subsolar gas. In the calculation, we assumed that Ne, Ar and Xe of initial concentrations equal to lunar soil[7] migrated through chondrule-sized materials heated at 1,600 K for 1,000 s. Even the energetic solar flare particles (up to 100 MeV per nucleon) can penetrate at most 1 mm into silicate matter[17], and hence noble-gas implantation would have occurred on fine grains of chondrule-precursor materials. If this is the case for the subsolar gases in chondrules, it is reasonable to expect that chondrules in other chondrite classes might also contain solar-type noble gas—in contrast to the limited reports that most chondrules in other chondrites are free of primordial noble gases[2–4]. Alternatively, chondrules in each chondrite class might have been produced from different precursor materials, and/or through different heating events during which solar gases trapped in the chondrule precursors would be lost due to high peak temperatures and a slow cooling rate.

On the other hand, astronomical observations have established that young solar-mass stars go through a phase of increased activity (the T Tauri phase), during which particle fluxes are considerably greater[18] than present solar fluxes. If abnormally high-energy particles were available during this active phase, they could have penetrated into the interior of chondrules; thus noble-gas implantation onto the surface of the EC parent body at the inner region of protosolar nebula could be responsible for the subsolar gas in chondrules. The elemental ratios of subsolar gas in chondrules can be explained by diffusive loss of solar-type noble gases, as mentioned above, while the subsolar-gas depletion in matrix portions could be the result of diffusion loss through small silicate grains (5 μm across). However, explaining the absence of noble gases in large opaque grains remains difficult.

Other mechanisms for trapping noble gases are adsorption on chondrule precursor materials, and solution into enstatite melt. The high concentrations of noble gases found in chondrules means that a high adsorption efficiency would have been required—this, in turn, requires very low temperatures. And such low-temperature adsorption would have brought a large amount of water into chondrule precursor materials: but there are no hydrous minerals in ECs[19], so we consider this mechanism unlikely. The solution of solar-nebula Ar in an enstatite melt[20] is also unlikely, because it would have required very high gas pressures during chondrule formation to compensate for the low solubility. □

Methods

Extraction efficiencies of the laser system were determined by comparing noble-gas concentrations obtained by the laser-ablation method with those obtained by a conventional total-melting method. Laser pits (~200 shots) were made at even intervals over the whole surface of thin slices (S6 and S8) as a check pattern, and gave a modal abundance of ablated minerals similar to that of each whole rock. The same samples as used for the laser-ablation method were heated at 1,800 °C for 20 min in a Mo crucible. The total-melting method guarantees complete degassing and thus no elemental fractionation. Based on the experiment, we estimated extraction efficiencies of 1.39, 1.09 and 1.08 for ^{36}Ar, ^{84}Kr and ^{132}Xe, respectively. Though a slight increase in the extraction efficiency for the lighter noble gas ^{36}Ar was observed, the mass releasing ^{36}Ar is only 40% larger than the melted material in each laser pit. Hence the spatial resolution of the laser system for ^{36}Ar is only 1.2 times as large as the apparent diameter of the laser pit—typically 50–80 μm.

Received 9 March; accepted 9 July 2001.

1. Rubin, A. E. Petrologic, geochemical and experimental constraints on models of chondrule formation. *Earth Sci. Rev.* **50,** 3–27 (2000).
2. Nakamura, T., Nagao, K. & Takaoka, N. Microdistribution of primordial noble gases in CM chondrites determined by in situ laser microprobe analysis: Decipherment of nebular processes. *Geochim. Cosmochim. Acta* **63,** 241–255 (1999).
3. Kim, J. S. & Marti, K. Distribution of some highly volatile elements in chondrules. *Meteoritics* **29,** 482 (1994).
4. Miura, Y. N. & Nagao, K. *Antarctic Meteorites* Vol. 22, 118–120 (National Inst. Polar Res., Tokyo, 1997).
5. Crabb, J. & Anders, E. Noble gases in E-chondrites. *Geochim. Cosmochim. Acta* **45,** 2443–2464 (1981).
6. Wacker, J. F. & Marti, K. Noble gas components in clasts and separates of the Abee meteorite. *Earth Planet. Sci. Lett.* **62,** 147–158 (1983).
7. Eberhardt, P. *et al.* Trapped solar wind noble gases in Apollo 12 lunar fines 12001 and Apollo 11 breccia 10046. *Proc. Lunar Planet. Sci. Conf.* **III,** 1821–1856 (1972).
8. Okazaki, R. *Origin of Noble Gases in Enstatite Chondrites and Ureilites: Evolutional Processes of Meteoritic Materials in the Early Solar System.* Thesis, Kyushu Univ. (2000).
9. Lewis, R. S., Srinivasan, B. & Anders, E. Host phases of a strange xenon component in Allende. *Science* **190,** 1251–1262 (1975).
10. Wieler, R., Anders, E., Baur, H., Lewis, R. S. & Signer, P. Characterisation of Q-gases and other noble gas components in the Murchison meteorite. *Geochim. Cosmochim. Acta* **56,** 2907–2921 (1992).
11. Crabb, J. & Anders, E. On the siting of noble gases in E-chondrites. *Geochim. Cosmochim. Acta* **46,** 2351–2361 (1982).
12. Kimura, M. & Lin, Y. Petrological and mineralogical study of enstatite chondrites with reference to their thermal histories. *Antarct. Meteorit. Res.* **12,** 1–18 (1999).
13. Okazaki, R., Takaoka, N., Nakamura, T. & Nagao, K. Cosmic-ray exposure ages of enstatite chondrites. *Antarct. Meteorit. Res.* **13,** 153–169 (2000).
14. Hewins, R. H. in *Chondrules and the Protoplanetary Disk* (eds Hewins, R. H., Jones, R. H. & Scott, E. R. D.) 257–264 (Cambridge Univ. Press, 1996).
15. Shu, F. H., Shang, H., Gounelle, M., Glassgold, A. E. & Lee, T. The origin of chondrules and refractory inclusions in chondritic meteorites. *Astrophys. J.* **548,** 1029–1050 (2001).
16. Hiyagon, H. *Preliminary Studies on Partition of Rare Gases between Crystals and Melts.* Thesis, Univ. Tokyo (1981).
17. Goswami, J. N., Lal, D. & Wilkening, L. L. Gas-rich meteorites: Probes for particle environment and dynamical processes in the inner solar system. *Space Sci. Rev.* **37,** 111–159 (1984).
18. Edwards, S., Ray, T. & Mundt, R. in *Protostars and Planets III* (eds Levy, E. H. & Lunine, J. I.) 567–602 (Univ. Arizona Press, Tucson, 1993).
19. Dodd, R. T. *Meteorites: a Petrologic-chemical Synthesis* (Cambridge Univ. Press, 1981).
20. Kirsten, T. Incorporation of rare gases in solidifying enstatite melts. *J. Geophys. Res.* **73,** 2807–2810 (1968).
21. Anders, E. & Grevesse, N. Abundances of the elements: Meteoritic and solar. *Geochim. Cosmochim. Acta* **53,** 197–214 (1989).
22. Ozima, M. & Podosek, F. A. *Noble Gas Geochemistry* (Cambridge Univ. Press, 1983).
23. Pepin, R. O. On the origin and early evolution of terrestrial planet atmospheres and meteoritic volatiles. *Icarus* **92,** 2–79 (1991).

Correspondence and requests for materials should be addressed to R.O. (e-mail: okazaki@eqchem.s.u-tokyo.ac.jp).

Fast heating of ultrahigh-density plasma as a step towards laser fusion ignition

R. Kodama*, P. A. Norreys†, K. Mima*, A. E. Dangor‡, R. G. Evans§, H. Fujita*, Y. Kitagawa*, K. Krushelnick‡, T. Miyakoshi*, N. Miyanaga*, T. Norimatsu*, S. J. Rose†, T. Shozaki*, K. Shigemori*, A. Sunahara*, M. Tampo*, K. A. Tanaka*‖, Y. Toyama*, T. Yamanaka* & M. Zepf‡

* *Institute of Laser Engineering, Osaka University, 2-6 Yamada-oka, Suita Osaka 565-0871, Japan*
† *Rutherford Appleton Laboratory, Chilton, Didcot OX11 0QX, UK*
‡ *Blackett Laboratory, Imperial College, London SW7 2BZ, UK*
§ *Department of Physics, University of York, Heslington, York YO1 5DD, UK*
‖ *Faculty of Engineering, Osaka University, 2-6 Yamada-oka, Suita Osaka 565-0871, Japan*

Modern high-power lasers can generate extreme states of matter that are relevant to astrophysics[1], equation-of-state studies[2] and fusion energy research[3,4]. Laser-driven implosions of spherical polymer shells have, for example, achieved an increase in density of 1,000 times relative to the solid state[5]. These densities are large

enough to enable controlled fusion, but to achieve energy gain a small volume of compressed fuel (known as the 'spark') must be heated to temperatures of about 10^8 K (corresponding to thermal energies in excess of 10 keV). In the conventional approach to controlled fusion, the spark is both produced and heated by accurately timed shock waves[4], but this process requires both precise implosion symmetry and a very large drive energy. In principle, these requirements can be significantly relaxed by performing the compression and fast heating separately[6–10]; however, this 'fast ignitor' approach[7] also suffers drawbacks, such as propagation losses and deflection of the ultra-intense laser pulse by the plasma surrounding the compressed fuel. Here we employ a new compression geometry that eliminates these problems; we combine production of compressed matter in a laser-driven implosion with picosecond-fast heating by a laser pulse timed to coincide with the peak compression. Our approach therefore permits efficient compression and heating to be carried out simultaneously, providing a route to efficient fusion energy production.

In order to heat the compressed matter separately, the heating energy needs to be deposited on a timescale of less than 10^{-11} s, as the compression disassembles on this timescale. This is the fast ignitor[7] approach. Present-day short-pulse laser technology is, in principle, capable of delivering sufficient energy in the required timescale, the largest laser to date having a peak power of 10^{15} W and pulse durations of 10^{-12} s (ref. 11). The laser energy is coupled to the highly compressed plasma via relativistic electrons that are efficiently generated when such an ultra-intense laser interacts with a high-density plasma[11–21]. The extremely large electromagnetic fields of the laser accelerate the electrons into the high-density matter. (For a laser with a wavelength of 1 μm, the typical conversion efficiency to the relativistic electrons has been measured to be about 30–40% at intensities above 10^{19} W cm^{-2} (refs 10, 21).) The electrons then propagate to the high-density region where they deposit their energy.

We have measured the propagation of such relativistic electrons in a solid, and the associated heating effects, by examining the interactions of a 40-TW/0.5-ps laser pulse with a solid aluminium target. Images (obtained using ultraviolet light; Fig. 1) showing heated regions were temporally separated from any other hydrodynamic heating such as shock-wave and/or heat-wave propagation processes by the use of a two-dimensional (2D) spatially resolved high-speed sampling camera[22]. The heating images indicate the propagation of the high-density electrons and collimation with a divergence (full-width at half-maximum) of 20–30°. The propagation of the large relativistic electron current is made possible by a return current of colder electrons that compensates the relativistic current almost perfectly. Magnetic fields associated with the current flow also serve to keep the electrons flowing initially in a narrow filament of the order of the laser spot diameter[23–25].

The experiments on heating of ultrahigh-density plasmas were performed on the Gekko XIII laser at the University of Osaka. This laser has 12 beams for nanosecond pulses, with a maximum energy of 15 kJ at 0.53 μm wavelength, and a synchronized subpicosecond-pulse beam with a power of 100 TW and a pulse energy of 60 J (ref. 26). Conventional laser fusion experiments are conducted with spherically symmetrical targets to achieve high densities and the formation of the spark. This geometry was also envisaged in the original fast ignitor proposal[7]. Potential problems with this approach are propagation losses and deflection[27] of the ultra-intense laser pulse in the plasma surrounding the highly compressed plasma, and the transport of the relativistic electron beam through a substantial length of a plasma[28]. Here we describe an experiment that departs from the original arrangement by inserting a gold cone (with an opening angle of 60°) into the shell (Fig. 2a; and S. Hatchett, unpublished work). The cone is designed to keep the propagation path of the short-pulse laser free from the plasma that forms around the imploding shell, thereby completely avoiding laser propagation issues. The cone tip was set at 50 μm from the centre of the shell, and ensures that the compressed dense plasma forms at the tip of the cone while leaving the cone intact. The proximity between the cone tip and the core plasma also reduces the sensitivity to electron-beam propagation instabilities and losses. The cone walls are on a radius from the centre of the shell, minimizing disruptions to the spherical symmetry of the implosion so that high densities can be achieved. The laser energy used for compression here was restricted to 1.2 kJ in 1-ns-long pulses to ensure that the internal energy of the core after compression (which is about 5% efficient) was of similar magnitude to the short-pulse laser energy available (~60 J). This facilitates the measurement of the core plasma heating.

Figure 2b is a typical X-ray image of the implosion of the

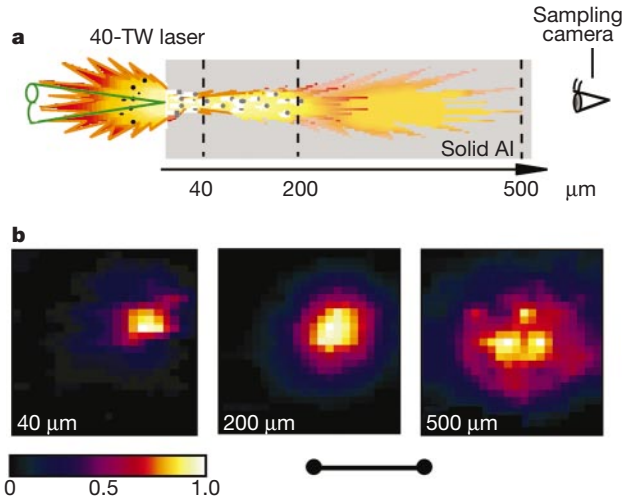

Figure 1 Ultraviolet images showing the heating of solid targets by relativistic electrons, and a sketch of the set-up used to obtain the images. **a**, 40-TW/20-J laser light was interacted with the Al solid target to create the electrons. The electrons heated the rear of the target, and this side of the target was imaged with the high-speed sampling camera. **b**, The heating images were obtained with the sampling camera for targets of different thickness (from 10 μm to 500 μm). The scale bar below the images corresponds to 200 μm on the target. The colour bar presents a linear intensity scale of the emission normalized by the peak intensity for each of the targets, to show clearly the difference in pattern. The relative peak intensities are about 5, 1 and 0.8 for the 40-μm, 200-μm and 500-μm targets, respectively.

deuterated-polystyrene (CD) shell without injection of the short-pulse laser. The imploded core plasma was created at the centre of the unimploded shell, close to the tip of the cone. The compressed density was estimated by time-resolved radiographic measurements—the compressed plasma was illuminated with X-rays from a secondary target, and the images were recorded on a multi-frame high-speed camera (100 ps per frame). The core plasma size was measured in this way to be 40–45 μm in diameter. In addition, the area corresponding to a density of 0.1–0.5 g cm^{-3} was obtained from the reduced brightness of the backlighting radiation surrounding the core using the calculated opacity (Fig. 2c). We know the initial mass of the shell target is 4×10^{-6} g, the mass of the absorbing area is 2.8×10^{-7} g from the opacity measurement, and the remaining mass after long-pulse laser ablation is 2.2×10^{-6} g (the ablated mass is 1.5×10^{-6} g) from both simulations and the experimental database on the mass ablation rate. From these, we estimate the average core density as 50–70 g cm^{-3} for the 40–45 μm core diameter. Given the non-uniformity of the laser illumination, the inferred density is consistent with that calculated using two-dimensional hydrodynamic simulations (an average density of 80–100 g cm^{-3}; Fig. 2c). The simulation also suggests that the insertion of the cone only marginally reduces the achieved compressed density (by about 20–30%) compared with full spherical implosion. This shows that implosions with a cone insert are compatible with achieving the high densities required for achieving fusion gain, while at the same time allowing for reliable and efficient coupling of the laser to the highly compressed plasma.

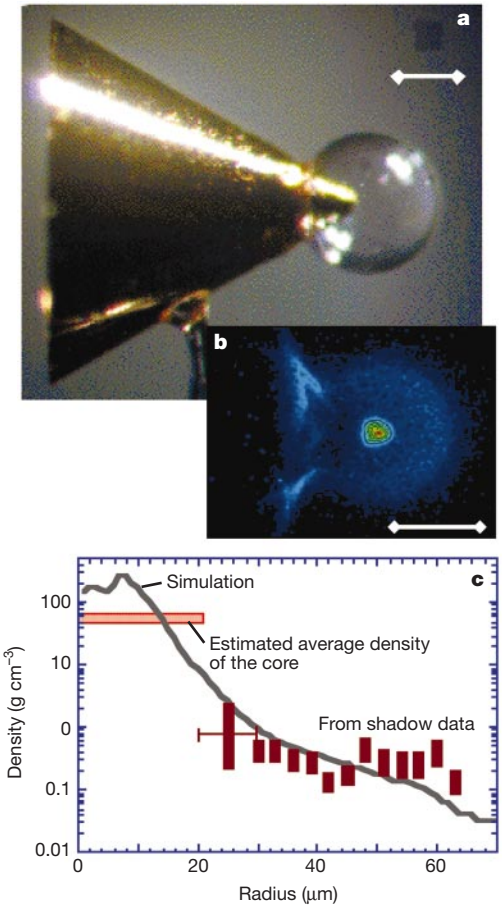

Figure 2 The implosion target for efficient heating of the highly compressed plasma, an X-ray image of the implosion, and the density profile of the plasma. The scale bars correspond to 250 μm on the target. **a**, A gold cone is attached to a deuterated-polystyrene (CD) shell (500 μm diameter, 7 μm wall thickness). 9 laser beams with a 1-ns duration are used to implode the shell at the tip of the cone. The 100-TW short-pulse laser is injected from the open side of the cone. **b**, Typical X-ray image showing the well imploded core plasma on the tip of the cone. The dimmer features correspond to the outline of the cone (left). The halo concentric with the bright core feature is emitted during the acceleration phase of the shell. **c**, Density profiles of the compressed plasma from the X-ray shadow, and a two-dimensional (2D) hydrodynamic simulation. The densities from the shadow are obtained by taking into account the opacity calculation. The errors shown are due to the spatial resolution. The 2D simulation code[29] is coupled with a one-dimensional (1D) simulation code including all the important physics. The initial conditions of the density and temperature given at the laser plasma interaction phase from the 1D code are introduced to the 2D code. In the code, incomplete spherical shock convergence and the interaction of the shell with the cone are treated, including long-wavelength hydrodynamic instability processes. However, no account is taken of shorter-wavelength perturbations of the shell caused at the acceleration phase.

We investigated the heating efficiency by injecting the 100-TW heating laser into the cone at the moment of maximum compression. The electron beam created by the 100-TW laser was measured with electron spectrometers during interactions with the cone target; we found that kT for the beam was 2–3 MeV. The conversion efficiency was obtained using the same laser with a plane target at a similar intensity (10^{19} W cm^{-2}); the energy of the electron beam was 18–24 J, representing 30–40% of the laser energy. To check the shape and divergence of the heated region associated with the electron beam in this new geometry, the 100-TW laser was injected into an identical cone target, but the tip of the cone touched an Al block (with a thickness of 200 μm at the point of contact), rather than being embedded in the CD shell. The heating area was elliptical in shape (40×25 μm^2; Fig. 3a), and the beam divergence was less than 20° from the size (130×80 μm^2) of the heated region on the back of the 200-μm Al. Figure 3b shows an image sequence of the core emission with the heating pulse injected at the time of maximum compression in the cone insert geometry. Figure 3c shows a similar sequence, but this time the heating pulse arrives 150 ps after the peak compression. The heating due to the short-pulse beam is clearly visible in the sequence in Fig. 3c: the first peak of the core emission coincides with the peak compression, and then decreases before peaking again after the injection of the heating pulse. The size of the emission region due to the peak in compression is about 30 μm, and increases to 50 μm after the injection of the heating pulse—in good agreement with the independent measurement of the heating region using the Al block.

Heating of the highly compressed plasma was quantified by

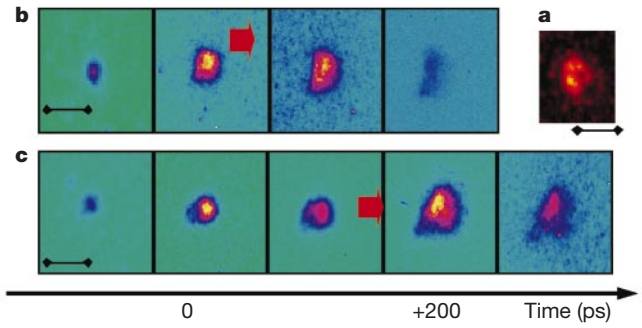

Figure 3 Time-integrated X-ray image of the short-pulse laser heating, and time-resolved X-ray images of the highly compressed plasma heated by the short-pulse laser. Time separation between each of the time-resolved images is 100 ps. The red arrows in the figure correspond to the timing of the short-pulse laser injection. The scale bar of the images shows 50 μm on the target. **a**, The image is observed from the beam-injection side of the cone attached to an Al block instead of the shell. **b**, The short-pulse laser was injected at a time close to the maximum compression of the shell. **c**, The injection timing is about 150 ps after the maximum compression. The heating by the short-pulse laser is temporally separated from the maximum compression heating of the shell.

Table 1 Neutron yield from the dense plasmas at different conditions

Target	E_i, no. of beams	E_s	N_y
Cone+shell	1.2 kJ, 9 beams	60 J	$(1–3)\times10^5$
Cone+shell	1.2 kJ, 9 beams	0	$(0.8–1)\times10^4$
Spherical shell only	2.6 kJ, 12 beams	0	$(2–3)\times10^5$

Thermal neutron yields N_y from the highly compressed plasmas are listed for different targets, implosion laser energy E_i and heating energy from the short-pulse laser E_s. The E_i is nominal energy measured after the focusing lens and through a random phase plate. These neutron yields indicates temperatures of several hundred eV.

measuring the increase in production of thermonuclear neutrons. Neutrons are generated by the fusion of two deuterium nuclei to a ^{3}He nucleus (d(d,n)^{3}He) in the imploded plasma, and provide a precise measurement of the plasma temperature. The neutron energy spectra were obtained using time-of-flight scintillator/photomultiplier detectors from two different angles. Peaks at an energy of 2.45 MeV are observed, corresponding to neutrons from a thermonuclear d(d,n)^{3}He reaction. The neutron time-of-flight spectrum in Fig. 4 shows a signal corresponding to a thermonuclear neutron yield of $(2\pm1)\times10^5$ neutrons, and was taken when the heating pulse was injected at maximum compression. This neutron yield was more than 10 times the numbers ($(9\pm1)\times10^3$) observed when no heating pulse was present or when the heating pulse was not timed to coincide with maximum compression. In order to replicate the neutron yield achieved at optimal timing in the conventional fashion (no heating pulse and a spherically symmetric implosion), a laser energy of 2.6 kJ was required to drive the implosion. Therefore the total energy required to achieve the observed neutron yield has been reduced by half, which is a clear demonstration of the increased efficiency that can be achieved by separating the compression and the heating phase in laser fusion experiments. These results, summarized in Table 1, provide (to our knowledge) the first clear evidence of effective heating of compressed plasma using an ultrahigh-intensity, short-pulse laser.

The efficiency of the energy coupling of the energetic electrons to the highly compressed plasma can be estimated from the neutron yield and the heated volume inferred from the X-ray images. In order to increase the neutron yield by a factor of 10–30, a temperature increase of about 120 eV (± 20%) is required for initial temperature regions of several hundred eV. The heated mass is estimated from the density (50–70 g cm^{-3}), and the volume is estimated from the size of the electron beam ($25\times40\,\mu m^2$) and the length of the high-density plasma (40 μm). Taking account of the beam divergence, the volume might be 1.2–1.3 times larger than this assumption. The heated distance might also be 30 μm from the core emission instead of 40 μm. Then the volume assumption will include an error of about ±30%. To heat uniformly the volume of density 50–70 g cm^{-3} ($25\times40\times40\,\mu m^3$) requires 12–16 J of the energetic electrons produced by the short-pulse laser. The total coupling efficiency of this laser to the compressed dense plasma could therefore be 20–27%, having estimation errors of ± 8% (12–35%) from the temperature and from the heated volume. This is an encouraging result.

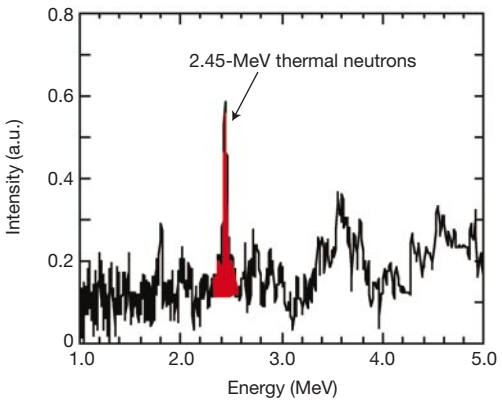

Figure 4 Neutron spectrum from the highly dense plasma heated by the short-pulse laser at the time of maximum compression. The peak at 2.45 MeV corresponds to neutrons from the thermonuclear deuterium–deuterium fusion reaction. The signal to noise ratio is ≥5.

Using the minimum 20% coupling efficiency observed in this experiment, we estimate the short-pulse laser energy needed to create a sufficiently large spark to ignite a deuterium–tritium (DT) fusion pellet ($T = 12$ keV, $\rho = 600$ g cm^{-3} and $\rho r = 0.4–0.6$ g cm^{-2}) to be 10–20 kJ (ref. 6), which seems feasible. Of course, we are still uncertain how the increase in the electron beam current will affect the propagation and energy deposition in the highly compressed DT plasma for a full-scale fusion experiment. For example, a fourfold increase in energy concentration is required as compared with this first demonstration experiment (as a smaller, 16-μm-diameter core needs to be heated due to the higher compression needed for ignition). Another issue to be resolved for the future ignition experiments is the fabrication of a uniform cryogenic fuel layer, such as a foam shell filled with liquid DT fuel. Nevertheless, we emphasized that the temperature of the energetic electrons used in our experiment is closely matched to the requirements of a full-scale fusion experiment. □

Received 4 May; accepted 6 July 2001.

1. Remington, B. A., Arnet, D., Drake, R. P. & Takabe, H. Modeling astrophysical phenomena in the laboratory with intense lasers. *Science* **284,** 1488–1493 (1999).
2. Ichimaru, S. & Kitamura, H. Pycnonuclear reactions in dense astrophysical and fusion plasmas. *Phys. Plasmas* **6,** 2649–2671 (1999).
3. Nuckolls, J., Wood, L., Thiessen, A. & Zimmerman, G. Laser compression of matter to super-high densities. *Nature* **239,** 139–142 (1972).
4. Lindl, J., McCrory, R. L. & Campbell, E. M. Progress toward ignition and burn propagation in inertial confinement fusion. *Phys. Today* **45,** 32–40 (1992).
5. Azechi, H. *et al.* High density compression experiments at ILE, Osaka. *Laser Part. Beams* **9,** 193–207 (1991).
6. Piriz, A. R. & Sanchez, M. M. Analytical model for the dynamics of fast ignition. *Phys. Plasmas* **5,** 2721–2726 (1998).
7. Tabak, M. *et al.* Ignition and high gain with ultrapowerful lasers. *Phys. Plasmas* **1,** 1626–1634 (1994).
8. Atzeni, S. Inertial fusion fast ignitor: Igniting pulse parameter window vs the penetration depth of the heating particles and the density of the precompressed fuel. *Phys. Plasmas* **6,** 3316–3326 (1999).
9. Norreys, P. *et al.* Experimental studies of the advanced fast ignitor scheme. *Phys. Plasmas* **7,** 3721–3726 (2000).
10. Kodama, R. *et al.* Fast ignition research at the institute of laser engineering Osaka University. *Phys. Plasmas* (in the press).
11. Perry, M. D. & Mourrou, G. Terawatt to petawatt subpicosecond lasers. *Science* **264,** 917–924 (1994).
12. Kruer, W. E. and Estabrook, K. JxB heating by very intense laser light. *Phys. Fluids* **28,** 430–432 (1985).
13. Brunel, F. Not-so-resonant, resonant absorption. *Phys. Rev. Lett.* **59,** 52–55 (1987).
14. Lefebvre, E. & Bonnaud, G. Transparency/opacity of a solid target illuminated by an ultrahigh-intensity laser pulse. *Phys. Rev. Lett.* **74,** 2002–2005 (1995).
15. Malka, G. & Miquel, J. L. Experimental validation of the linear theory of stimulated Raman scattering driven by a 500-fs laser pulse in a preformed underdense plasma. *Phys. Rev. Lett.* **74,** 4655–4658 (1996).
16. Pukhov, A. & Meyer-ter-Vehn, J. Laser hole boring into overdense plasma and relativistic electron currents for fast ignition of ICF targets. *Phys. Rev. Lett.* **79,** 2686–2689 (1997).
17. Key, M. H. *et al.* Hot electron production and heating by hot electrons in fast ignitor research. *Phys. Plasmas* **5,** 1966–1972 (1998).
18. Kodama, R. *et al.* Long-scale jet formation with specularly reflected light in ultraintense laser-plasma interactions. *Phys. Rev. Lett.* **84,** 674–677 (2000).
19. Santala, M. I. K. *et al.* Effect of the plasma density scale length on the direction of fast electrons in relativistic laser-solid interactions. *Phys. Rev. Lett.* **84,** 1459–1463 (2000).
20. Tanaka, K. A. *et al.* Studies of ultra-intense laser plasma interactions for fast ignition. *Phys. Plasmas* **7,** 2014–2022 (2000).
21. Wharton, K. B. *et al.* Experimental measurements of hot electrons generated by ultraintense ($>10^{19}$W/cm^2) laser plasma interactions on solid-density targets. *Phys. Rev. Lett.* **81,** 822–825 (1998).
22. Kodama, R. *et al.* Development of a two-dimensional space-resolved high speed sampling camera. *Rev. Sci. Instrum.* **70,** 625–628 (1999).
23. Davies, J. R., Bell, A. R. & Tatarakis, M. Magnetic focusing and trapping of high-intensity laser generated fast electrons at the rear of solid targets. *Phys. Rev. E* **59,** 6032–6036 (1999).
24. Tatarakis, M. *et al.* Plasma formation on the front and rear of plastic targets due to high-intensity laser-generated fast electrons. *Phy. Rev. Lett.* **81,** 999–1002 (1998).
25. Honda, M., Meyer-ter-Vehn, J. & Pukhov, A. Collective stopping and ion heating in relativistic-electron-beam transport for fast ignition. *Phys. Rev. Lett.* **85,** 2128–2131 (2000).
26. Kato, Y *et al.* Fast ignition and related plasma physics issues with high-intensity lasers. *Plasma Phys. Control. Fusion* **39,** 145–151 (1997).

27. Duda, B. J., Hemker, R. G., Tzeng, K. C. & Mori, W. B. A long-wavelength hosing instability in laser-plasma interactions. *Phys. Rev. Lett.* **83,** 1978–1981 (1999).
28. Hain, S., Cornolti, F. & Opower, H. Hydrodynamic models and schemes for fast ignition. *Laser Part. Beams* **17,** 245–263 (1999).
29. Sunahara, A., Takabe, H & Mima, K. 2D simulation of hydrodynamic instability in ICF stagnation phase. *Fusion Eng. Design* **44,** 163–169 (1999).

Acknowledgements

We thank the mm-Wave Technology Centre at the Rutherford Appleton Laboratory, and the target fabrication, laser operation and data acquisition groups at ILE Osaka University. This work was supported by the Japan Society for the Promotion of Science, and the UK Royal Society.

Correspondence and requests for materials should be addressed to R.K. (e-mail: ryo@ile.osaka-u.ac.jp).

Formation of ordered ice nanotubes inside carbon nanotubes

Kenichiro Koga*, G. T. Gao†‡, Hideki Tanaka§ & X. C. Zeng†

* *Department of Chemistry, Fukuoka University of Education, Fukuoka 811-4192, Japan*
† *Department of Chemistry and Center for Materials and Analysis, University of Nebraska, Lincoln, Nebraska 68588, USA*
§ *Department of Chemistry, Okayama University, 3-1-1, Tsushima, Okayama 700-8530 Japan*

Following their discovery[1], carbon nanotubes have attracted interest not only for their unusual electrical and mechanical properties, but also because their hollow interior can serve as a nanometre-sized capillary[2–7], mould[8–11] or template[12–14] in material fabrication. The ability to encapsulate a material in a nanotube also offers new possibilities for investigating dimensionally confined phase transitions[15]. Particularly intriguing is the conjecture[16] that matter within the narrow confines of a carbon nanotube might exhibit a solid–liquid critical point[17] beyond which the distinction between solid and liquid phases disappears. This unusual feature, which cannot occur in bulk material, would allow for the direct and continuous transformation of liquid matter into a solid. Here we report simulations of the behaviour of water encapsulated in carbon nanotubes that suggest the existence of a variety of new ice phases not seen in bulk ice, and of a solid–liquid critical point. Using carbon nanotubes with diameters ranging from 1.1 nm to 1.4 nm and applied axial pressures of 50 MPa to 500 MPa, we find that water can exhibit a first-order freezing transition to hexagonal and heptagonal ice nanotubes, and a continuous phase transformation into solid-like square or pentagonal ice nanotubes.

Carbon nanotubes can be wetted by liquids[4] whose surface tension does not exceed about 200 mN m^{-1}. Thus, in principle, pure water can be drawn into open-ended nanotubes by capillary suction[5]. Once inside, water molecules are expected to form quasi-one-dimensional (Q1D) structures that might form new phases of ice, different from the 13 polymorphic phases of bulk ice identified experimentally thus far[18]. We carried out molecular dynamics (MD) simulations at constant temperature (T) and axial-pressure (P_{zz}) of water confined within 'armchair'[19] (R,R) single-walled carbon nanotubes (SWCNs). We used nanotubes with indices R = 14–18, corresponding to tubes with diameters of 11.1, 11.9, 12.6, 13.4 and 14.2 Å, respectively. The phase behaviour of the confined water was examined in several series of the MD simulations, each series corresponding to an isobaric path or an isothermal path in the P_{zz}–T phase diagram at a given R (see Methods for details).

The first series of simulations follows an isobaric path of 50 MPa. The temperature was lowered stepwise starting from 320 K or higher, where the system is in a liquid state, to 240 K or lower. The potential energy of water in each type of SWCN is plotted in Fig. 1. In the wide SWCNs (16,16) and (17,17), the potential energy drops abruptly (Fig. 1c and d) on cooling and jumps sharply on heating. This marked hysteresis-loop behaviour signifies a first-order phase transition. Structural analysis reveals that the low-T phase is a Q1D n-gonal 'ice nanotube' composed of orderly stacked n-membered water rings[20], where n = 6 (hexagonal) in (16,16) and n = 7 (heptagonal) in (17,17) SWCNs. In both types of nanotube, the molar volume of water decreases during the liquid-to-ice nanotube transition; that is, the confined water shrinks on freezing. In the widest SWCN (18,18), however, crystallization was not observed within the timescale of simulation. In the narrower SWCNs (14,14) and (15,15), the potential energy also drops markedly on cooling below 300 K, but the change is not as sharp as in the wider nanotubes. Structural analysis shows that confined water has liquid-like disordered structure at high T but turns into solid-like ordered structure at low T—a square nanotube in (14,14) and a pentagonal nanotube in (15,15) SWCN. At 240 K, the calculated diffusion constants (along the axial direction) are $D = 3 \times 10^{-10}$ cm^2 s^{-1} in the (14,14) SWCN, and $D < 1 \times 10^{-10}$ cm^2 s^{-1} in the (15,15) SWCN, which are comparable to D of bulk ice[21]. At 300 K, $D = 1 \times 10^{-5}$ cm^2 s^{-1} and $D = 2 \times 10^{-5}$ cm^2 s^{-1} respectively. More interestingly, besides the less sharp charge in the potential energy, the hysteresis loop was not observed in the cooling and heating process, a signature of continuous transformation from liquid-like to solid-like state of water.

In real-world experiments, the atomic structures of Q1D crystals can be determined by using transmission electron microscopy[11]. Simulations provide this information directly. Figure 2 displays snapshots of the Q1D n-gonal (n = 4–6) ice nanotubes and the corresponding Q1D liquid phases inside the (14,14), (15,15) and

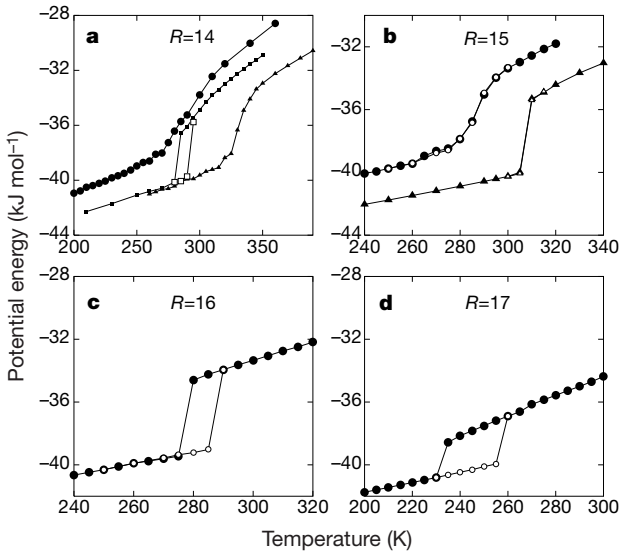

Figure 1 Potential energy against temperature for water confined in four types of single-walled carbon nanotube. The nanotubes are armchair (R,R) SWCNs, where R = 14–17 (**a**–**d**, respectively). The potential energy is due to the water–water intermolecular interactions, and the water–SWCN interaction energy is excluded. The applied axial pressure is 50 MPa (circles), 200 MPa (squares), and 500 MPa (triangles). Filled and unfilled symbols indicate the cooling and heating process, respectively.

‡ Present address: Department of Chemistry, U.S. Naval Academy, Annapolis, Maryland 21402, USA